Gondwana Research 89 (2021) 168–176

Contents lists available at ScienceDirect

Gondwana Research

journal homepage: www.elsevier.com/locate/gr

Receiver function investigation of crustal structure in the Malawi and Luangwa rift zones and adjacent areas

Muchen Sun [a,b,*], Stephen S. Gao [b], Kelly H. Liu [b], Kevin Mickus [c], Xiaofei Fu [d,e], Youqiang Yu [a]

[a] State Key Laboratory of Marine Geology, Tongji University, Shanghai 200092, China
[b] Geology and Geophysics Program, Missouri University of Science and Technology, Rolla, MO 65409, USA
[c] Department of Geography, Geology, and Planning, Missouri State University, Springfield, MO, USA
[d] Heilongjiang Institute of Technology, Harbin, Heilongjiang 150050, China
[e] College of Earth Science and Research Institute of Unconventional Oil and Gas, Northeast Petroleum University, Daqing, Heilongjiang 163318, China

ARTICLE INFO

Article history:
Received 19 March 2020
Received in revised form 8 August 2020
Accepted 15 August 2020
Available online 6 October 2020

Handling Editor: N. Rawlinson

Keywords:
Crustal structure
Malawi Rift Zone
Luangwa Rift Zone
Receiver function

ABSTRACT

Stacking over 2300 *P*-to-*S* receiver functions recorded by 33 SAFARI (Seismic Arrays for African Rift Initiation) broadband seismic stations that we installed in the vicinity of the Malawi and Luangwa rift zones (MRZ and LRZ, respectively) reveals significant variations of crustal thickness (32.8–46.3 km) and V_p/V_s (1.69–1.85). The resulting crustal stretching factor is about 1.05–1.08 for the MRZ, which is approximately 10–40% lower than that observed in the mature segments of the East African Rift System (EARS). The low stretching factor is consistent with the general absence of volcanism in the MRZ, and the relatively high V_p/V_s (≥ 1.81) beneath the southern MRZ, when combined with observations from previous studies, indicate the possible existence of crustal partial melting, elevated temperatures or fluid-filled deep crustal faults that are likely associated with lithospheric stretching. In sharp contrast with the southern MRZ, low V_p/V_s measurements in the range of 1.69–1.72 are observed along the western boundary of the northern MRZ, which could be attributable to the infiltration of magma-derived CO_2 into the crust. The LRZ shows negligible crustal thinning and a V_p/V_s that is comparable to the globally averaged value for continental crust, suggesting a complete post-rifting recovery of crustal properties in terms of crustal thickness and V_pV_s.

1. Introduction

A typical continental rift is a fault-bounded narrow valley where the entire lithosphere has been pulled apart under extension (Sengor and Burke, 1978; Gregory, 1894). As an archetypal example of continental rifts, the East Africa Rift System (EARS), which extends from the northern Red Sea to the southern terminus of the Malawi rift zone (MRZ), is an ideal natural laboratory for investigating rifting mechanisms and the characteristics of continental rifts in various stages. Relative to most of the other segments of the EARS, the Cenozoic MRZ of the EARS and the nearby Paleozoic-Mesozoic Luangwa Rift Zone (LRZ; Ebinger et al., 2017) have been less adequately investigated. Consequently, the magnitude and extent of crustal deformation, the existence of partial melting or mafic intrusion in the crust, and important characteristics such as the depth penetration and possible CO_2 infiltration (Roecker et al., 2017) of the seismically active boundary faults, remain enigmatic.

Laboratory investigations of crustal rock samples (Holbrook et al., 1992) suggest that under average crustal temperature and pressure conditions, felsic, intermediate, and mafic rocks have V_p/V_s values of smaller than 1.76, between 1.76 and 1.81, and greater than 1.81, respectively. The existence of crustal partial melting can lead to a higher V_p/V_s due to a greater reduction of V_s than V_p (Greenfield et al., 2016). Similarly, intensive intrusion of mantle materials into the crust can also increase the bulk crustal V_p/V_s (Christensen, 1996). An increasing number of mineral physical and observational studies have suggested that CO_2 released from the mantle through deep and steep lithospheric faults can significantly reduce crustal V_p/V_s (Julian et al., 1998; Lee et al., 2016; Parmigiani et al., 2016; Roecker et al., 2017). Specifically, it has been suggested that CO_2 can decrease V_p through its strong effect on the pore-fluid compressibility of porous crustal rocks, and consequently, reduce the crustal V_p/V_s (Ito et al., 1979; Mavko and Mukerji, 1995). Therefore, observations of V_p/V_s values that are below the normal felsic rock value of 1.76 may suggest the presence of magma-derived CO_2, as well as the existence of lithospheric faults acting as conduits for the CO_2 (Lee et al., 2016).

In this study, we measure spatial variations of crustal thickness and V_p/V_s using *P*-to-*S* receiver functions (RFs) recorded at 33 broadband seismic stations (Gao et al., 2013), to unveil crustal characteristics and

* Corresponding author at: State Key Laboratory of Marine Geology, Tongji University, Shanghai 200092, China.
E-mail address: ms7yf@mst.edu (M. Sun).

https://doi.org/10.1016/j.gr.2020.08.015
1342-937X/

possible effects of CO_2 infiltration and partial melting on crustal V_p/V_s beneath the MRZ and LRZ and adjacent areas.

2. Tectonic setting

The Cenozoic MRZ is the southernmost segment of the magma-poor western branch of the EARS. It separates the Nubian plate and the Rovuma microplate (Fig. 1) and originated approximately 25 Ma (Roberts et al., 2012). The Rungwe Volcanic Province located at the northern tip of the rift zone is the only volcanic province within the MRZ (Ebinger et al., 1993). Kinematic GPS studies (Saria et al., 2014; Stamps et al., 2018) indicated that the spreading rate between the Nubian plate and the Rovuma microplate decreases gradually from the northern tip (2.2 mm/yr) to the southern tip (1.5 mm/yr) of the MRZ. One of the most controversial issues beneath the MRZ is the existence of thermal upwelling from the lower mantle. Broadband seismic studies of the MRZ reveal a normal mantle transition zone thickness (Reed et al., 2016) and a NE-SW oriented seismic azimuthal anisotropy (Reed et al., 2017) under the rift, suggesting that there is no significant rift-related mantle flow and detectable influence of an active plume in the vicinity of the mantle transition zone (Yu et al., 2020). Geodynamic modeling studies also inferred a lack of observable thermal upwelling from the lower mantle beneath the MRZ, and favor an upper mantle origin of rifting (Stamps et al., 2014, 2015). In contrast, a recent seismic anisotropy study (Tepp et al., 2018) attributes the NE oriented azimuthal anisotropy observed in the MRZ to horizontal mantle flow that is enhanced by weak thermal upwelling from the lower mantle beneath southern Africa. Similarly, the existence of an active mantle plume from the lower mantle beneath southern Africa has been suggested by seismic tomography (Ritsema et al., 1999; Mulibo and Nyblade, 2013) and geodynamic modeling studies (Lithgow-Bertelloni and Silver, 1998; Gurnis et al., 2000).

Relative to the mantle, the crust beneath most part of the MRZ has been inadequately studied. A recent RF study for the northern MRZ and the Rungwe Volcanic Province (Borrego et al., 2018) suggests a bulk felsic to intermediate crustal composition and small variation of crustal thickness, and concludes that crustal thinning in the northern MRZ, if it exists, must be highly focused beneath the center of the rifted basin. Based on the vertical gradient of shear wave velocities, an ambient noise tomography (ANT) study suggests that the crustal thickness beneath the MRZ ranges from 36 to 40 km (Wang et al., 2019).

Another major tectonic feature in East Africa is the Permo-Triassic LRZ, which has been reactivated probably by the same stress field responsible for the formation of the Cenozoic EARS (Banks et al., 1995; Fritz et al., 2013). The Luangwa rifting started in the earliest Permian and ended in the Triassic (Daly et al., 1989; Banks et al., 1995; Fritz et al., 2013). The southwestern segment of the LRZ follows the ENE-trending Mwembeshi Shear Zone, which separates the Proterozoic Irumide Belt and the South Irumide Belts (SIB), while its northeastern portion is situated in the Irumide Belt (Fig. 1). Geochronological studies by Johnson et al. (2005, 2006) indicate that different magmatic events resulted in a significant distinction of crustal characteristics between

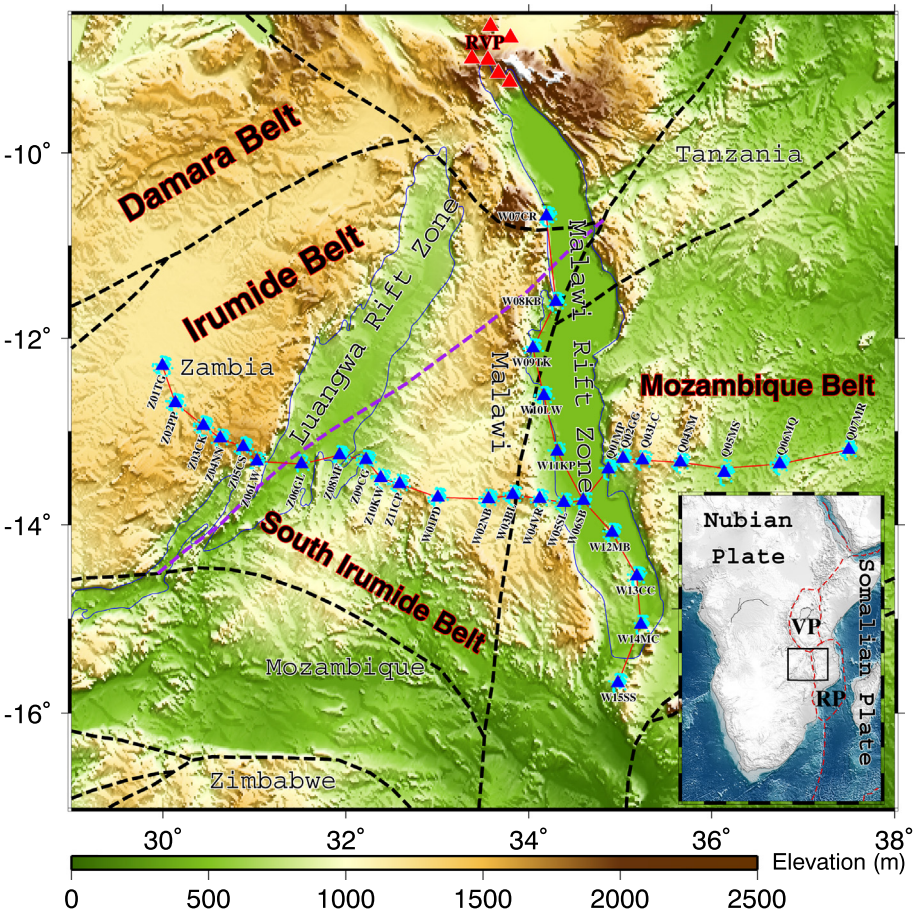

Fig. 1. Topographic map of the study area showing the distribution of seismic stations (blue triangles) used in the study, volcanoes (red triangles) and major tectonic features. The light cyan dots are ray-piercing points of *P*-to-*S* conversions at the depth of 41.5 km. The dashed lines show the tectonic boundaries (Craig et al., 2011), among which the purple dashed line is the Mwembeshi Shear Zone. Two red solid lines are the trajectories of the W-E and S-N profiles, respectively. RVP: Rungwe Volcanic Province. The rectangle in the inset map indicates the study area. VP: Victoria Microplate; RP: Rovuma Microplate.

these two neighboring orogenic belts. The Mwembeshi Shear Zone separates the lithosphere between the Irumide Belt and SIB, which is evidenced by the observation of an electrically conductive discontinuity in the mantle (Sarafian et al., 2018). This conductive discontinuity might represent a suture zone which is a result of collision between two lithospheric fragments after subduction of an oceanic slab beneath the Irumide Belt (Johnson et al., 2007; Sarafian et al., 2018). Previous integrated studies consider that the left lateral movement on the Mwembeshi Shear Zone dominated the development of the LRZ, while subsequent right lateral movement resulted in rifting inversions (Daly et al., 1989; Orpen et al., 1989; Banks et al., 1995).

3. Data and methods

The teleseismic (epicentral distance ranging from 30° to 100°) data used in the study were recorded by 33 stations (Fig. 1) that we installed in Malawi, Mozambique, and Zambia over a 2 year period (2012–2014) as a component of the SAFARI (Seismic Arrays for African Rift Initiation; Gao et al., 2013) project. One of these stations (Q05MS) is a combination of two nearby stations Q05MJ and Q05ML. To balance the quality and quantity of the selected data, a variable cut-off magnitude (M_c) was set by $M_c = 5.2 + (\Delta - \Delta_{min})/(\Delta_{max} - \Delta_{min}) - D/D_{max}$ where Δ and D are the epicentral distance in degree and focal depth in kilometer, respectively, $\Delta_{min} = 30°$, $\Delta_{max} = 100°$, and $D_{max} = 700$ km (Liu and Gao, 2010). A four-pole, two-pass Butterworth bandpass filter with corner frequencies of 0.04 and 0.8 Hz was applied to the three-component seismograms, which were windowed 20 s before and 50 s after the theoretical first *P*-wave arrival based on the IASP91 Earth model (Kennett and Engdahl, 1991). If the signal to noise ratio (S/N) of the first arrival on the vertical component was greater than 4.0, the filtered seismograms were converted into radial *P*-to-*S* RFs following the procedure of Ammon (1991) with a water level value of 0.03. The S/N is obtained by $\max|A_s|/|\overline{A}_n|$, where $\max|A_s|$ is the maximum absolute amplitude on the vertical seismogram 8 s before and 17 s after the predicted IASP91 arrival time for the first *P*-wave, and $|\overline{A}_n|$ is the average absolute amplitude in the time window of 10–20 s before the predicted *P*-wave arrival time (Liu and Gao, 2010). The resulting RFs for each of the stations were inspected visually to reject the ones without a clear first *P*-wave arrival in the first 2 s window. A total of 2307 high-quality radial RFs from 241 events (Fig. 2) were selected for determining crustal thickness (H) and V_p/V_s (κ).

3.1. H-κ stacking

Following the H-κ stacking procedure of Zhu and Kanamori (2000), the selected RFs were moveout corrected and stacked to grid-search for the optimal pair of the crustal thickness and V_p/V_s, which corresponds to the maximum stacking amplitude. We search for the maximum amplitude in the depth range of 25–50 km with an interval of 0.1 km, and in the V_p/V_s range of 1.60–1.95 with an interval of 0.01. The weighting factors used in this study are $w_1 = 0.5$, $w_2 = 0.4$ and $w_3 = 0.1$ for *Pms*, *Ppms* and *Psms*, respectively. In comparison, Kachingwe et al. (2015) used two different sets of weighting factors ($w_1 = 0.4$, $w_2 = 0.3$, $w_3 = 0.3$ and $w_1 = 0.5$, $w_2 = 0.5$, $w_3 = 0.0$) for different stations. Two sets of weighting factors ($w_1 = 0.4$, $w_2 = 0.3$, $w_3 = 0.3$, and $w_1 = 0.6$, $w_2 = 0.1$, $w_3 = 0.3$) were also used by Borrego et al. (2018). For two (W07CR and Z06GL) of the 33 stations, which have two peaks with comparable amplitudes on the H-κ plot, the search ranges were adjusted to select the peak corresponding to an H-κ pair that is comparable to the neighboring stations. H-κ plots for all the 33 stations are shown in Figs. S1-S33. In this study, a crustal average *P*-wave velocity of 6.1 km/s was chosen for the H-κ stacking, which is consistent with the IASP91 Earth model. It is worth noting that the average crustal velocity assumed has a positive correlation with the resulting crustal thickness, and a negative correlation with the resulting V_p/V_s. Specifically, a 1% increase of average crustal velocity assumed can lead to an ~0.46 km increase in the resulting crustal thickness and an ~0.0024 reduction in the resulting V_p/V_s, respectively (Nair et al., 2006). Subsequently, following a bootstrap resampling procedure (Efron and Tibshirani, 1986), the average and standard deviation of the measurements for each station were calculated using 10 iterations. For each bootstrap iteration, $1–1/e = 63\%$ independent RFs were chosen randomly. About 60% of the chosen ones were then duplicated so that the total number of the new set of RFs is the same as that of the original set.

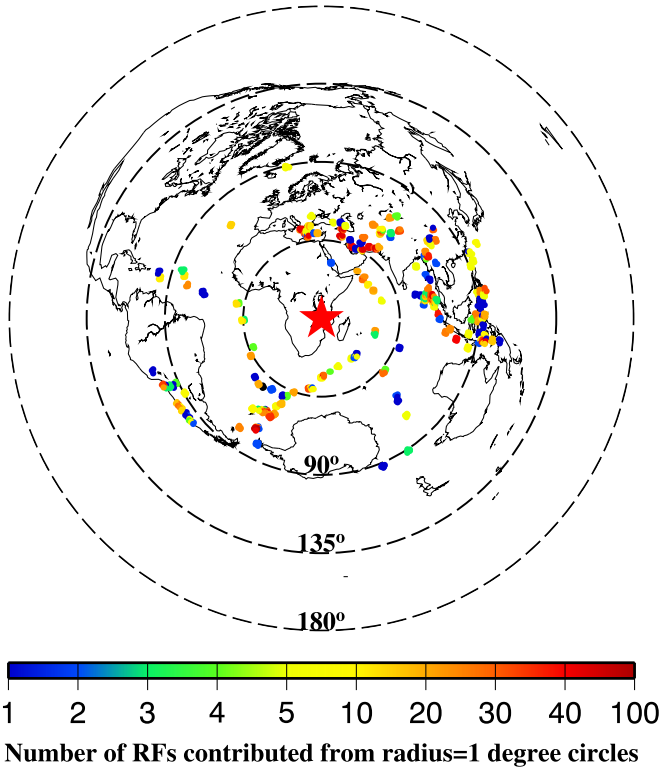

Fig. 2. Spatial distribution of earthquake source areas. Each dot represents a radius = 1° circular area. The distance between neighboring circles is 1°. The colour of the dot represents the number of used RFs originated from earthquakes in the circle. The radius of the concentric dashed circles centered at the central part of the study area (star) indicates the epicentral distance.

A delay time of approximately 0.5 s of the first arrival (Fig. S34) and a large negative pulse after the first arrival in the RFs are observed at one of the stations (Z06GL) located in the LRZ (Fig. 3a), which is part of a strongly attenuative reverberation series most likely caused by the presence of a low-velocity (relative to that of the bedrock) sedimentary layer (Yu et al., 2015). Such reverberations could lead to erroneous crustal thickness and V_p/V_s measurements (Yeck et al., 2013; Yu et al., 2015). For this station, we determined the two-way travel time of the reverberations and designed a sedimentary layer effect-removal filter in the frequency domain (Yu et al., 2015) to remove the reverberations and to isolate the *P*-to-*S* converted phases from the Moho (Fig. 3).

Because results from H-κ stacking were obtained under the assumption that the crust is an isotropic, horizontal single layer, they represent vertically and azimuthally averaged values over the entire crust. While crustal anisotropy and Moho tilting can lead to azimuthally dependent H and κ measurements, the decent azimuthal coverage of the events (Fig. 2) suggests that crustal anisotropy and Moho tilting may have insignificant effects on the results. Another possible source of uncertainty is that if an underplating magmatic layer with an impedance contrast that is greater than that across the Moho exists, the crustal thickness determined by the H-κ stacking method represents the depth from the surface to the top of the underplating magmatic layer rather than the true crustal thickness (Fontaine et al., 2015).

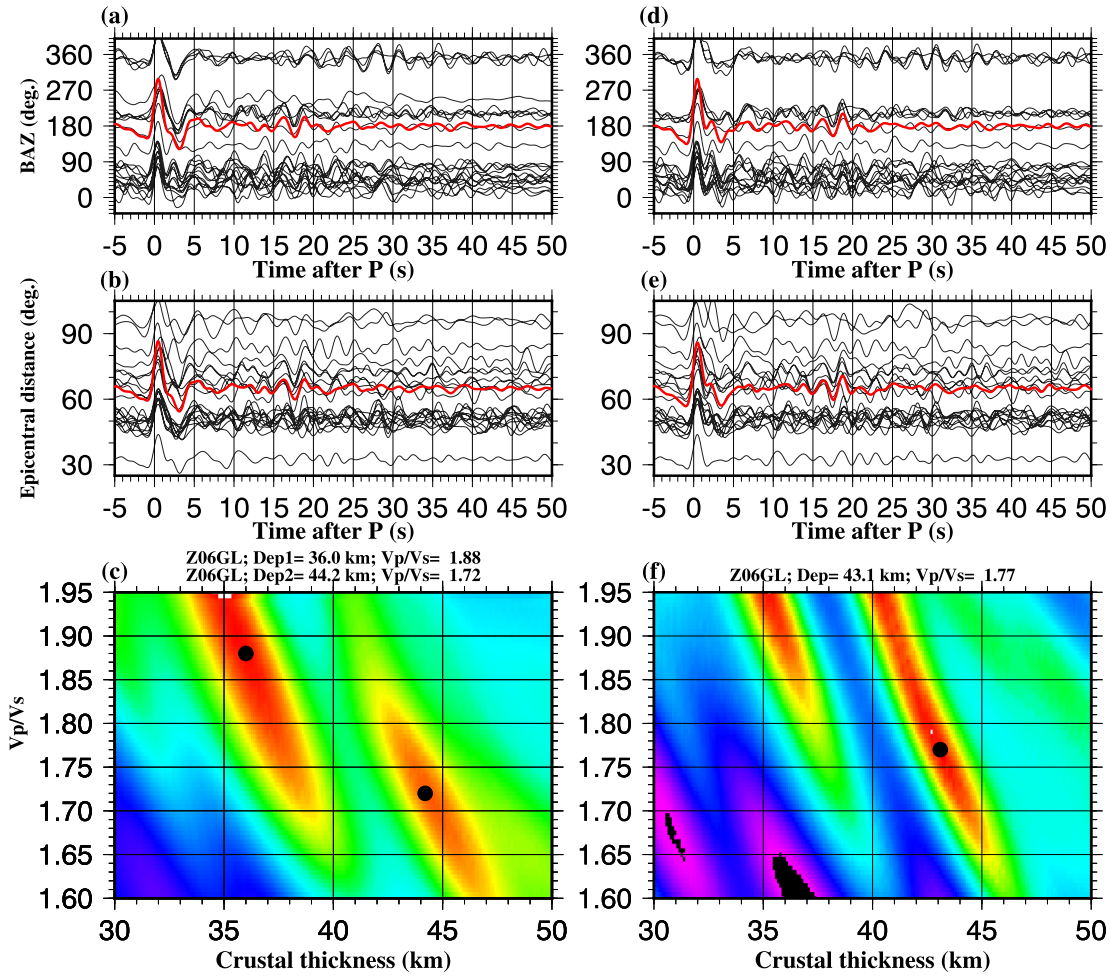

Fig. 3. (a) Original RFs from Station Z06GL plotted against back azimuth (BAZ). The red trace is the result of simple time domain summation of the individual RFs. (b) Original RFs from Station Z06GL plotted against epicentral distance. (c) H-κ stacking using the raw RFs shown in Fig. 3a. The dot denotes the maximum stacking amplitude. (d) Same as Fig. 3a but for RFs after removing the reverberations using the approach of Yu et al. (2015). (e) Same as Fig. 3b but for RFs after removing the reverberations. (f) H-κ stacking using the filtered RFs shown in Fig. 3d.

3.2. RF migration

To create a spatially continuous image of the Moho, we migrated the RFs and projected them into a rift orthogonal (W-E) and a rift parallel (S-N) profile, respectively, for RFs with a distance between the profile and the ray-piercing point (computed at 41.5 km depth) less than 50 km (Reed et al., 2014). To produce the cross-sections, the RF raypaths were computed using an assumed average crustal V_p of 6.1 km/s and the optimal average crustal V_p/V_s value for each station obtained from the H-κ stacking. We then divided the 25–55 km depth range of the Earth along the profile into rectangular blocks of 1° (longitude for the W-E profile, and latitude for the S-N profile) by 1 km (vertical) with a horizontal and vertical moving step of 0.1° and 0.1 km, respectively. The average amplitude of the RFs with raypaths in each of the rectangular blocks was calculated and the stacked RFs were normalized by the maximum amplitude in the 25–55 km depth range.

4. Results

Robust *P*-to-*S* arrivals are obtained from the migrated RFs (Figs. 4 and 5), enabling reliable determinations of crustal thickness and V_p/V_s beneath the vast majority of the stations.

4.1. Crustal thickness and V_p/V_s from H-κ stacking

The resulting crustal thicknesses vary from 32.8 km beneath the northern part of the MRZ to 46.3 km beneath the Mozambique belt with an average of 41.4 ± 2.7 km (Fig. 6), and the V_p/V_s values range from 1.69 to 1.85 with an average value of 1.75 ± 0.04 (Fig. 7 and Table S1). Along the rift-orthogonal profile, the crustal thickness in the MRZ is 2–3 km thinner than the surrounding orogenic belts (Figs. 4 and 6). The Mozambique Belt has an average thickness of 41.9 ± 2.8 km and V_p/V_s of 1.78 ± 0.04. The average crustal thickness of the SIB is 43.6 ± 0.8 km, while the V_p/V_s measurements have an average value of 1.75 ± 0.02. H-κ stacking from 6 stations in the Irumide Belt leads to an average crustal thickness of 41.0 ± 1.9 km and V_p/V_s of 1.73 ± 0.02. For the two stations situated in the LRZ, the crustal thickness is 43.1 km at Z06GL and 44.9 km at Z08MF, and the V_p/V_s are 1.77 and 1.75, respectively.

Along the rift-parallel profile, the averaged crustal thickness is 39.4 ± 2.7 km (Fig. 6). The thinnest crust (32.8 km) was found beneath Station W07CR at the northern end of the profile, while the thickest crust (42.0 km) was observed at Station W12MB in the central part of the MRZ (Fig. 6). The resulting V_p/V_s values observed beneath MRZ fall within the range of 1.69–1.82 with an average of 1.74 ± 0.05 (Fig. 7). Small V_p/V_s values were revealed at 5 stations (W07CR, W08KB, W09TK, W10KP, and W11LW) in the northern half of the S-N profile,

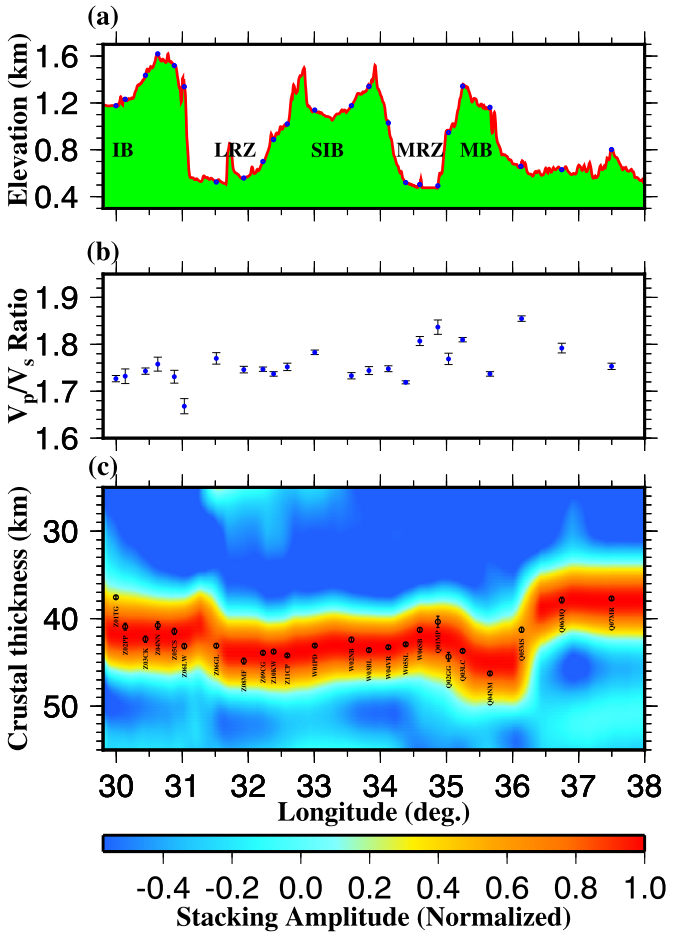

Fig. 4. (a) Surface elevation, (b) V_p/V_s measurements, and (c) migrated RF profile along the rift-orthogonal profile. The black dots in (c) indicate results from H-κ stacking, and the vertical bars in (b) and (c) represesnt the standard deviation of the measurements. Note that due to horizontal smoothing, some discrepancies (e.g., Station Z01TG) exist between the results of H-κ stacking and RF migration shown in (c). IB: Irumide Belt; LRZ: Luangwa Rift Zone; SIB: South Irumide Belt; MRZ: Malawi Rift Zone; MB: Mozambique Belt.

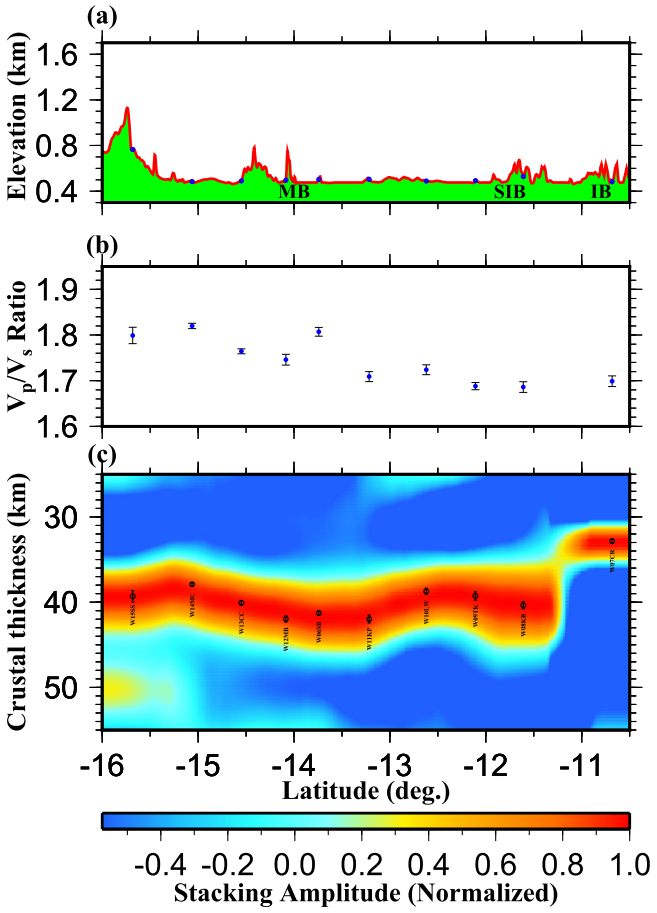

Fig. 5. Same as Fig. 4 but for the rift-parallel profile. Note that the narrow high-stacking-amplitude band at the northern end of the profile is caused by the low amplitude of the *Pms* phase (Fig. S7).

ranging from 1.69 to 1.72, with an average of 1.70 ± 0.01. The resulting crustal thickness measurements beneath the southern half of the S-N profile vary from 37.9 km to 42.0 km with an average of 40.1 ± 1.6 km, and the V_p/V_s values range from 1.75 to 1.82 with an average of 1.79 ± 0.03.

The measurements of crustal thickness along two profiles in this study are consistent with that from several neighboring stations in previous RF studies using H-κ stacking and joint inversion of RFs and Rayleigh-wave dispersion (Kachingwe et al., 2015; Borrego et al., 2018). Using data from 39 broadband seismic stations and an assumed crustal V_p of 6.5 km/s, the crustal structure beneath southern Africa was investigated using RFs (Kachingwe et al., 2015). Three of their stations were approximately along our profiles. A crustal thickness of 34.7 ± 0.7 km was reported at Station MZM, which was located between our stations W07CR and W08KB at which crustal thicknesses of 32.8 ± 0.3 km and 40.4 ± 0.4 km were obtained, respectively. However, the V_p/V_s (1.81 ± 0.04) reported at Station MZM (Kachingwe et al., 2015) is larger than those obtained at W07CR (1.70 ± 0.01) and W08KB (1.69 ± 0.01). One of the possible causes of the disparity might be related to the fact that MZM was located ~25 km west of the MRZ boundary fault, while W07CR and W08KB were near the fault and thus the small V_p/V_s may reflect CO_2 infiltration, as discussed in Section 5.2.

The crustal thickness and V_p/V_s determined at Station ZOMB are 38.3 ± 0.7 km and 1.79 ± 0.03 (Kachingwe et al., 2015), respectively,

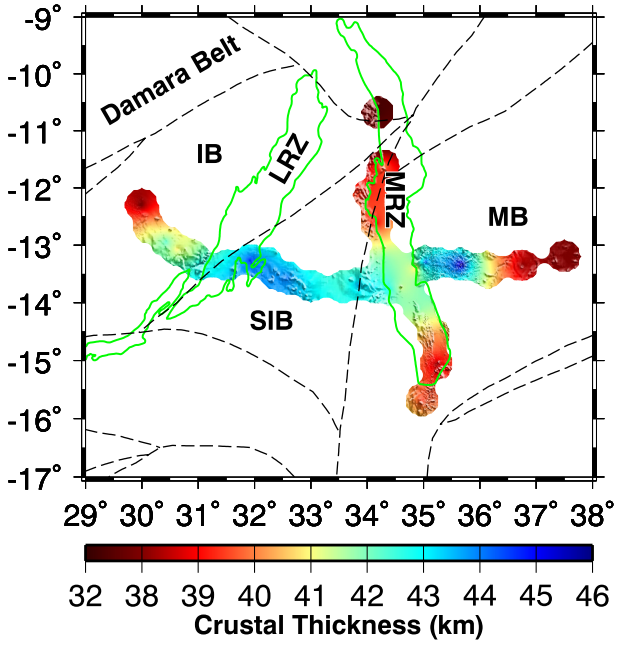

Fig. 6. Distribution of resulting crustal thickness. Station locations and names can be found in Fig. 1.

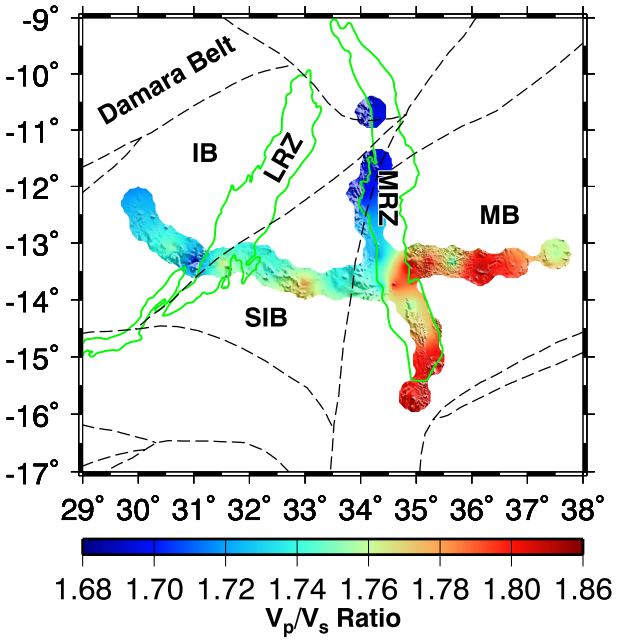

Fig. 7. Distribution of resulting V_p/V_s measurements.

while our results are 37.9 ± 0.2 km and 1.82 ± 0.01 at Station W14MC which was co-sited with ZOMB. The crustal thickness and V_p/V_s reported by Kachingwe et al. (2015) beneath Station SERJ are 45.2 ± 1.6 km and 1.70 ± 0.03, which are similar to the 42.4 ± 0.4 km and 1.74 ± 0.01 values reported at a nearby station (Station Z03CK) in this study. Crustal thicknesses from jointly inverting *P*-wave RFs and surface wave dispersion curves at stations MZM, ZOMB and SERJ are 40, 38, and 43 km, respectively (Kachingwe et al., 2015).

The RF study of Borrego et al. (2018), which focused on the northern MRZ and the Rungwe Volcanic Province, had two stations near our stations. When an average crustal V_p of 6.5 km/s was used, the crustal thickness at LIVA is 37.3 ± 1.3 km, which is about 4 km larger than the crustal thickness of 32.8 ± 0.27 km observed by our adjacent Station W07CR, and the V_p/V_s at Station LIVA (1.71 ± 0.05) is comparable with that obtained by Station W07CR (1.70 ± 0.01). Similarly, for Station THAN, the reported crustal thickness is 43.8 ± 4.9 km, which is also about 4 km larger than the crustal thickness of 40.4 km that we observed at neighboring Station W08KB. The V_p/V_s values between the two stations are comparable (1.67 ± 0.07 at THAN and 1.69 ± 0.01 at W08KB). Note that Borrego et al. (2018) used three average crustal V_p of 6.3 km/s, 6.5 km/s and 6.8 km/s in their RF study, which are higher than the value of 6.1 km/s that we used. As mentioned in Section 3.1, a larger V_p leads to a greater crustal thickness (Nair et al., 2006).

4.2. Moho depth variation from migrated RFs

The spatial variation of crustal thickness and its correspondence with surface elevation is visible on the migrated and laterally smoothed RF profiles (Figs. 4 and 5). Along the rift-orthogonal profile (Fig. 4), the western boundary of the LRZ separates the LRZ with a thick crust and the Irumide Belt with relatively thin crust. Contrasting to the commonly observed correspondence between thicker crust and higher elevations, the Irumide Belt, which has a thinner crust, is characterized by an elevation that is more than 1 km higher than the LRZ. Additionally, although the Irumide Belt and the SIB have similar elevations, the crust beneath the latter is a few km thicker.

A different relationship between crustal thickness and surface elevation is revealed in the eastern half of the rift-orthogonal profile, where a thicker crust corresponds to a higher elevation. For instance, the MRZ, which has the lowest elevation in the study area, corresponds to a crustal thinning of a few kilometers relative to the adjacent SIB, and the high elevation area on the Mozambique Belt adjacent to the MRZ is characterized by a thick crust. A sudden thinning of the crust further east corresponds to a significant elevation reduction.

The along-rift variation of crustal thickness is delineated by the migrated RFs (Fig. 5). The major features include a crustal thickening at the high-elevation southern terminus of the MRZ, as well as a sudden crustal thinning beneath the northern end of the profile. Caution must be taken for stations north of 14°S, the stations were located on the western edge of the MRZ, while the rest of the stations along the S-N profile were approximately in the axial area (Fig. 1). Therefore, if the area with the maximum crustal thinning is limited underneath the surface expression of the rift, the observed crustal thickness beneath the northern stations might be larger than the axial area. However, it is worth to realize that the difference in the resulting crustal thickness between Station W05SL, which, similar to the northern stations, was on the rift shoulder, and Station W06SB, which was approximately in the axial area, is less than 2 km.

4.3. Spatial variation of stacking amplitudes

The *R* value, which is the maximum stacking amplitude on the H-κ plot relative to the stacking amplitude of the direct *P*-wave, is a measure of the sharpness of the Moho and can also be affected by a number of other parameters including the velocity contrast across the Moho (e.g., Nair et al., 2006; Liu and Gao, 2010). For the entire study area, the average *R* value is 0.12 ± 0.04, which is close to the average value of 0.14 measured in southern Africa (Nair et al., 2006). To quantify possible changes in crustal properties between the rift and outside the rift, we estimate the *R* value along the S-N profile for RFs with an eastward back azimuth (BAZ) that traversing the MRZ (R_e) and those with a westward BAZ traversing the western rift flank (R_w). Fig. 8 suggests that at the three stations located in the northern and a station (W06SB) in the middle parts of the profile, the *R* values calculated by RFs from the east are significantly lower than that from the west, while comparable R_e and R_w values are observed for most of the other stations.

5. Discussion

5.1. Constraints on crustal magmatic intrusion and partial melting beneath the MRZ

In this study, a relatively flat Moho (39.4 ± 2.7 km) was found under most stations in the MRZ including the central and southern parts of the MRZ. The average crustal thickness observed beneath the Mozambique Belt and SIB are 41.9 ± 2.8 km and 43.6 ± 0.8 km, respectively, which are consistent with the ≥40 km results from a recent ANT study (Wang et al., 2019). Therefore, along the rift-orthogonal profile, the crustal thickness in the MRZ is 2–3 km thinner than the surrounding orogenic belts (Figs. 4 and 6), leading to a stretching factor (β) factor of about 1.05–1.08, which is about 10–40% lower than that observed in the mature segments of the EARS (Stuart et al., 2006; Reed et al., 2014; Plasman et al., 2017). Here, the stretching factor is defined as the ratio between the initial crustal thickness and the final crustal

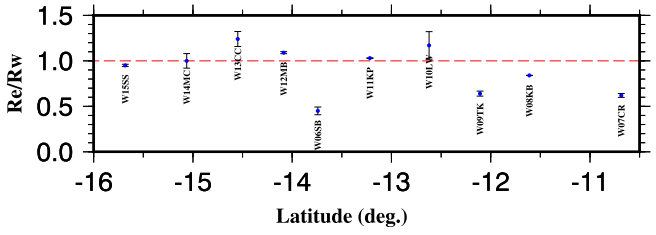

Fig. 8. The ratio between the *R* values calculated by RFs from the east (R_e) and those from the west (R_w).

thickness (Park, 1997). This stretching factor seems to indicate that, relative to other parts of the EARS, crustal thinning within the MRZ is relatively minor even within the central portion of the MRZ. This relatively low magnitude crustal thinning beneath the MRZ is consistent with the absence of volcanism on the surface except for the Rungwe Volcanic Province.

It must be mentioned that stations on the northern half of the S-N profile are mostly located on the western shoulder of the MRZ, and thus the crust beneath the rift axis is likely thinner than the H values observed at those stations. Similarly, Borrego et al. (2018) observed negligible crustal thinning beneath the uplifted flanks of the northern MRZ, suggesting that crustal thinning in the northern MRZ, if it exists, must be highly focused beneath the rift axis.

In contrast to the small variations of crustal thickness along the axis of the MRZ, the resulting V_p/V_s values observed within the MRZ vary greatly from 1.69 at the northernmost part to 1.84 in the central part of the MRZ (Fig. 7), implying significant along-rift variations of crustal composition, degree of partial melting, or temperature. The high V_p/V_s (≥ 1.81) determined at stations Q01MP, W06SB, and W14MC (Fig. 7), which are situated in the central and southern parts of the MRZ, implies the possible existence of magmatic intrusion in the lower crust, partial melting, elevated temperature or fluid-filled deep faults in the crust beneath some areas of the MRZ. Higher-than-normal V_s in the crust is expected, if the high V_p/V_s is caused by magmatic intrusion in the crust from the mantle. However, the recent ANT study (Wang et al., 2019) revealed lower-than-normal V_s in the crust beneath these areas. All these observations, when combined with the evidence of the absence of crustal thickening from magmatic addition observed in this study (Fig. 4), are inconsistent with the possibility of the presence of magmatic intrusion of high-density mantle material into the crust beneath the central and southern parts of the MRZ.

A RF study (Reed et al., 2016) using the SAFARI data suggests a normal mantle transition zone thickness, indicating the absence of the present-day influence of hot mantle upwelling from the lower mantle which would result in a thinner than normal MTZ due to the positive and negative Clapeyron slopes of the 410 and 660 km discontinuities, respectively. Additionally, shear wave splitting studies (Silver et al., 2001; Reed et al., 2017) observed overall NE-SW fast orientations in the vicinity of the MRZ, which is consistent with the absolute plate motion, suggesting the absence of a rift-parallel or rift-orthogonal small-scale flow system which has been suggested in some other continental rifts such as the Baikal Rift Zone (Gao et al., 1994, 1997). The lack of expected reduction on the splitting times observed at stations in the MRZ also suggests the absence of strong mantle upwelling beneath the MRZ (Reed et al., 2017). These observations suggest that the high V_p/V_s values could be related to partial melting, elevated temperatures or fluid-filled deep faults induced by lithospheric stretching rather than ascending magma from an active mantle plume rising from the lower mantle.

5.2. Infiltration of magma-derived CO_2 in the crust beneath the northern MRZ

Anomalously low V_p/V_s values ranging from 1.69 to 1.72 with an average value of 1.70 ± 0.01 were determined at five stations (W07CR, W08KB, W09TK, W10LW, and W11KP) along the western boundary of the MRZ. The most commonly cited cause for such low V_p/V_s values is the presence of rocks with a high silicon content (Christensen, 1996), which, to our knowledge, is not found by previous studies in the study area. A recently proposed alternate mechanism for low V_p/V_s is magma-derived CO_2 in the crustal porous rock (Roecker et al., 2017). CO_2 can decrease V_p through its strong effect on the pore-fluid compressibility of the crustal porous rock, and consequently, reduce the crustal V_p/V_s, an observation that is supported by both elasticity theory (Mavko and Mukerji, 1995) and experiments (Ito et al., 1979). Based on the observation that the V_p/V_s in the area with massive CO_2 outgassing beneath Mammoth Mountain (California) is about 9% lower than surrounding rocks, Julian et al. (1998) also suggested that the anomaly low V_p/V_s could be a diagnostic feature of magma-derived CO_2 degassing.

Magma-derived CO_2 can be released from the sub-continental lithosphere through deeply penetrating extensional fault systems (e.g., Julian et al., 1998; Parmigiani et al., 2016; Foley and Fischer, 2017; Roecker et al., 2017), which potentially makes the EARS an important source area in the Earth deep carbon cycle (Burton et al., 2013). Parmigiani et al. (2016) suggest that a magmatic volatile phase is prone to migrate from the crystal-rich regions to the crystal-poor parts, and accumulate large volumes of low density bubbles at the roof of the crystal-poor magma reservoir. Therefore, the deep boarder and intra-rift faults beneath the rift zones, if they connect to the magma reservoir in the sub-continental lithosphere, could be infiltrated by the magma-derived volatiles (Foley and Fischer, 2017; Roecker et al., 2017). The high CO_2 flux data in the fault zones reveals that the deep lithospheric fault system in the EARS does act as permeable conduits for transporting magma-derived CO_2 (Lee et al., 2016).

Considering the enormous quantity of recently recognized CO_2 outgassing along the faults in the EARS (Lee et al., 2016) and similar observations of low V_p/V_s values along the edges of the EARS in northern Tanzania and southern Kenya (Roecker et al., 2017), we speculate that a viable explanation for the anomalously low V_p/V_s observed in the northern part of the MRZ is caused by the infiltration of magma-derived CO_2 in the crust.

5.3. Post-rifting recovery of crustal thickness and V_p/V_s of the LRZ

Unlike the tectonically active MRZ, the resulting crustal thickness beneath the Paleozoic-Mesozoic LRZ, the southern part of which was developed in the Mwembeshi Shear Zone, is not significantly thinner than that beneath the adjacent orogenic belts. It has been widely recognized that regional compression can lead to cessation of rifting. If the compressional stress persists for a longer time, it can result in recovery of the original crustal thickness (Stein et al., 2018), leading to rift inversion. Additionally, reduction in rifting-related high temperature anomalies and disappearance of crustal partial melting may cause the reduction of the V_p/V_s anomaly associated with rifting.

The formation of the LRZ and its subsequent inversion can be related to strike slip movements along the Mwembeshi Shear Zone. Left lateral movement associated with continental collision along the Mwembeshi Shear Zone formed the LRZ in earliest Permian times, while later right lateral movements, which changed regional stress pattern from extension to compression in the vicinity of the LRZ, led to post-rifting inversion (Banks et al., 1995). The observed negligible crustal thinning and insignificant variation of V_p/V_s beneath the LRZ relative to the surrounding area suggest that post-rifting recovery of the LRZ has possibly completed since the cessation of the rifting event. Finally, it is worth mentioning that the ANT study of Wang et al. (2019) observed a possible crustal thinning of a few kilometers beneath the LRZ. This minor disparity is possibly caused by the limited number and spatial distribution of the stations in the LRZ and the fact that the two stations near the LRZ were not located in the center of the rift. Additional investigations, preferably using data from a 2-D broadband seismic network, are needed to determine the degree of post-rifting recovery of the crust in the LRZ.

6. Conclusions

Crustal thickness and V_p/V_s beneath 33 SAFARI stations located along two profiles in the vicinity of the MRZ and LRZ were imaged by stacking 2307 high-quality RFs. The crustal thickness measurements are generally consistent with sparsely spaced previous measurements. The new observations show that relative to the adjacent orogenic belts, the crust beneath the MRZ is thinned by about 3 km. This low magnitude crustal stretching is consistent with the absence of volcanisms in the main portions of the MRZ. Some areas in the MRZ show a high crustal

V_p/V_s of 1.81 or greater, which, when combined with the observations from other broadband seismic studies, may indicate the existence of partial melting, elevated temperatures or fluid-filled deep crustal faults probably associated with lithospheric stretching. One of the most significant observations from this study is the spatially consistent low V_p/V_s measurements in the range of 1.69–1.72 along the western edge of the northern MRZ, which could be interpreted by the infiltration of magma-derived CO_2 into the crust. Based on the negligible crustal thinning and insignificant variation of V_p/V_s beneath the LRZ relative to the surrounding area, we propose that the post-rifting inversion of the LRZ has possibly completed, and the recent reactivation of tectonic activities in the failed rift represents localization of regional strain along preexisting zones of mechanical weakness in the rifted crust.

Supplementary data to this article can be found online at https://doi.org/10.1016/j.gr.2020.08.015.

CRediT authorship contribution statement

M.S. wrote the paper with help from all the co-authors. S.G., K.L., and Y.Y. wrote the computer programs and provided financial supports.

Declaration of competing interest

The authors declare that they have no known competing financial interests or personal relationships that could have appeared to influence the work reported in this paper.

Acknowledgments

We thank the IRIS DMC for archiving the data used in the study, and the Portable Array Seismic Studies of the Continental Lithosphere Instrument Center for providing equipment and logistical support. All the data used in the study were obtained from the IRIS DMC (last accessed: August 2018; doi:https://doi.org/10.7914/SN/XK_2012). Field assistance provided by Cory Reed, Shane Ingate, Patrick R. N. Chindandali, Belarmino Massingue, Hassan Mdala, and Daniel Mutamina, as well as by various government agencies and universities in Malawi, Mozambique, and Zambia are greatly appreciated. We also thank F. R. Fontaine, an anonymous reviewer and Editor N. Rawlinson for suggestions that significantly improved the manuscript. This study was partially supported by the U.S. National Science Foundation under grants 1009946 and 1460516 to S.G. and K.L., and by the China Postdoctoral Science Foundation to M.S. under grant 2019M661607.

References

Ammon, C.J., 1991. The isolation of receiver effects from teleseismic *P*-waveforms. Bull. Seismol. Soc. Am. 81 (6), 2504–2510.

Banks, N.L., Bardwell, K.A., Musiwa, S., 1995. Karoo rift basins of the Luangwa Valley, Zambia. Geol. Soc. Lond., Spec. Publ. 80 (1), 285–295. https://doi.org/10.1144/GSL.SP.1995.080.01.13.

Borrego, D., Nyblade, A.A., Accardo, N.J., Gaherty, J.B., Ebinger, C.J., Shillington, D.J., et al., 2018. Crustal structure surrounding the northern Malawi rift and beneath the Rungwe Volcanic Province, East Africa. Geophys. J. Int. 215 (2), 1410–1426. https://doi.org/10.1093/gji/ggy331.

Burton, M.R., Sawyer, G.M., Granieri, D., 2013. Deep carbon emissions from volcanoes. Rev. Mineral. Geochem. 75 (1), 323–354. https://doi.org/10.2138/rmg.2013.75.11.

Christensen, N.I., 1996. Poisson's ratio and crustal seismology. J. Geophys. Res. Solid Earth 101 (B2), 3139–3156. https://doi.org/10.1029/95JB03446.

Craig, T.J., Jackson, J.A., Priestley, K., McKenzie, D., 2011. Earthquake distribution patterns in Africa: their relationship to variations in lithospheric and geological structure, and their rheological implications. Geophys. J. Int. 185 (1), 403–434. https://doi.org/10.1111/j.1365-246X.2011.04950.x.

Daly, M.C., Chorowicz, J., Fairhead, J.D., 1989. Rift basin evolution in Africa: the influence of reactivated steep basement shear zones. Geol. Soc. Lond., Spec. Publ. 44 (1), 309–334. https://doi.org/10.1144/GSL.SP.1989.044.01.17.

Ebinger, C.J., Deino, A.L., Tesha, A.L., Becker, T., Ring, U., 1993. Tectonic controls on rift basin morphology: evolution of the Northern Malawi (Nyasa) Rift. J. Geophys. Res. Solid Earth 98 (B10), 17821–17836. https://doi.org/10.1029/93JB01392.

Ebinger, C.J., Keir, D., Bastow, I.D., Whaler, K., Hammond, J.O., Ayele, A., et al., 2017. Crustal structure of active deformation zones in Africa: implications for global crustal processes. Tectonics 36 (12), 3298–3332. https://doi.org/10.1002/2017TC004526.

Efron, B., Tibshirani, R., 1986. Bootstrap methods for standard errors, confidence intervals, and other measures of statistical accuracy. Stat. Sci. 54–75.

Foley, S.F., Fischer, T.P., 2017. An essential role for continental rifts and lithosphere in the deep carbon cycle. Nat. Geosci. 10 (12), 897. https://doi.org/10.1038/s41561-017-0002-7.

Fontaine, F.R., Barruol, G., Tkalcic, H., Wolbern, I., Rumpker, G., Bodin, T., Haugmard, M., 2015. Crustal and uppermost mantle structure variation beneath La Reunion hotspot track. Geophys. J. Int. 203 (1), 107–126. https://doi.org/10.1093/gji/ggv279.

Fritz, H., Abdelsalam, M., Ali, K.A., Bingen, B., Collins, A.S., Fowler, A.R., et al., 2013. Orogen styles in the East African Orogen: a review of the Neoproterozoic to Cambrian tectonic evolution. J. Afr. Earth Sci. 86, 65–106. https://doi.org/10.1016/j.jafrearsci.2013.06.004.

Gao, S., Davis, P.M., Liu, H., Slack, P.D., Zorin, Y.A., Mordvinova, V.V., Kozhevnikov, V.M., Meyer, R.P., 1994. Seismic anisotropy and mantle flow beneath the Baikal Rift Zone. Nature 371, 149–151. https://doi.org/10.1038/371149a0.

Gao, S., Davis, P.M., Liu, H., Slack, P.D., Rigor, A.W., Zorin, Y.A., Mordvinova, V.V., Kozhevnikov, V.M., Logatchev, N.A., 1997. SKS splitting beneath continental rift zones. J. Geophys. Res. Solid Earth 102, 22,781–22,797. https://doi.org/10.1029/97JB01858.

Gao, S.S., Liu, K.H., Reed, C.A., Yu, Y., Massinque, B., Mdala, H., et al., 2013. Seismic arrays to study African rift initiation. EOS Trans. Am. Geophys. Union 94 (24), 213–214. https://doi.org/10.1002/2013EO240002.

Greenfield, T., White, R.S., Roecker, S., 2016. The magmatic plumbing system of the Askja central volcano, Iceland, as imaged by seismic tomography. J. Geophys. Res. Solid Earth 121 (10), 7211–7229. https://doi.org/10.1002/2016JB013163.

Gregory, J.W., 1894. Contributions to the physical geography of British East Africa. Geogr. J. 4, 289–315.

Gurnis, M., Mitrovica, J.X., Ritsema, J., van Heijst, H.J., 2000. Constraining mantle density structure using geological evidence of surface uplift rates: the case of the African superplume. Geochem. Geophys. Geosyst. 1 (7). https://doi.org/10.1029/1999GC000035.

Holbrook, W.S., Mooney, W.D., Christensen, N.I., 1992. The seismic velocity structure of the deep continental crust. Continental Lower Crust 23, 1–43.

Ito, H., DeVilbiss, J., Nur, A., 1979. Compressional and shear waves in saturated rock during water-steam transition. J. Geophys. Res. Solid Earth 84 (B9), 4731–4735. https://doi.org/10.1029/JB084iB09p04731.

Johnson, S.P., Rivers, T., De Waele, B., 2005. A review of the Mesoproterozoic to early Palaeozoic magmatic and tectonothermal history of south-Central Africa: implications for Rodinia and Gondwana. J. Geol. Soc. 162 (3), 433–450. https://doi.org/10.1144/0016-764904-028.

Johnson, S.P., De Waele, B., Liyungu, K.A., 2006. U-P_b sensitive high-resolution ion microprobe (SHRIMP) zircon geochronology of granitoid rocks in eastern Zambia: terrane subdivision of the Mesoproterozoic Southern Irumide Belt. Tectonics 25 (6). https://doi.org/10.1029/2006TC001977.

Johnson, S.P., De Waele, B., Tembo, F., Katongo, C., Tani, K., Chang, et al., 2007. Geochemistry, geochronology and isotopic evolution of the Chewore-Rufunsa Terrane, Southern Irumide Belt: a Mesoproterozoic continental margin arc. J. Petrol. 48 (7), 1411–1441. https://doi.org/10.1093/petrology/egm025.

Julian, B.R., Pitt, A.M., Foulger, G.R., 1998. Seismic image of a CO_2 reservoir beneath a seismically active volcano. Geophys. J. Int. 133 (1), F7–F10. https://doi.org/10.1046/j.1365-246X.1998.1331540.x.

Kachingwe, M., Nyblade, A., Julia, J., 2015. Crustal structure of Precambrian terranes in the southern African subcontinent with implications for secular variation in crustal genesis. Geophys. J. Int. 202 (1), 533–547. https://doi.org/10.1093/gji/ggv136.

Kennett, B.L.N., Engdahl, E.R., 1991. Traveltimes for global earthquake location and phase identification. Geophys. J. Int. 105 (2), 429–465. https://doi.org/10.1111/j.1365-246X.1991.tb06724.x.

Lee, H., Muirhead, J.D., Fischer, T.P., Ebinger, C.J., Kattenhorn, S.A., Sharp, Z.D., Kianji, G., 2016. Massive and prolonged deep carbon emissions associated with continental rifting. Nat. Geosci. 9 (2), 145. https://doi.org/10.1038/ngeo2622.

Lithgow-Bertelloni, C., Silver, P.G., 1998. Dynamic topography, plate driving forces and the African superswell. Nature 395 (6699), 269. https://doi.org/10.1038/26212.

Liu, K.H., Gao, S.S., 2010. Spatial variations of crustal characteristics beneath the Hoggar swell, Algeria, revealed by systematic analyses of receiver functions from a single seismic station. Geochemistry, Geophysics, Geosystems 11 (8). https://doi.org/10.1029/2010GC003091.

Mavko, G., Mukerji, T., 1995. Seismic pore space compressibility and Gassmann's relation. Geophysics 60 (6), 1743–1749. https://doi.org/10.1190/1.1443907.

Mulibo, G.D., Nyblade, A.A., 2013. The P and S wave velocity structure of the mantle beneath eastern Africa and the African superplume anomaly. Geochem. Geophys. Geosyst. 14 (8), 2696–2715. https://doi.org/10.1002/ggge.20150.

Nair, S.K., Gao, S.S., Liu, K.H., Silver, P.G., 2006. Southern African crustal evolution and composition: constraints from receiver function studies. J. Geophys. Res. Solid Earth 111 (B2). https://doi.org/10.1029/2005JB003802.

Orpen, J.L., Swain, C.J., Nugent, C., Zhou, P.P., 1989. Wrench-fault and half-graben tectonics in the development of the Palaeozoic Zambezi Karoo Basins in Zimbabwe - the "Lower Zambezi" and "Mid-Zambezi" basins respectively - and regional implications. Journal of African Earth Sciences (and the Middle East) 8 (2–4), 215–229. https://doi.org/10.1016/S0899-5362(89)80026-0.

Park, R. G., 1997. Foundation of structural geology. (3rd Ed.) Psychology Press. p. 64.

Parmigiani, A., Faroughi, S., Huber, C., Bachmann, O., Su, Y., 2016. Bubble accumulation and its role in the evolution of magma reservoirs in the upper crust. Nature 532 (7600), 492. https://doi.org/10.1038/nature17401.

Plasman, M., Tiberi, C., Ebinger, C., Gautier, S., Albaric, J., Peyrat, S., et al., 2017. Lithospheric low-velocity zones associated with a magmatic segment of the Tanzanian Rift, East Africa. Geophys. J. Int. 210 (1), 465–481. https://doi.org/10.1093/gji/ggx177.

Reed, C.A., Almadani, S., Gao, S.S., Elsheikh, A.A., Cherie, S., Abdelsalam, M., Thurmond, A., Liu, K.H., 2014. Receiver function constraints on crustal seismic velocities and partial melting beneath the Red Sea rift and adjacent regions, Afar Depression. J. Geophys. Res. Solid Earth 119, 2138–2152. https://doi.org/10.1002/2013JB010719.

Reed, C.A., Liu, K.H., Chindandali, P., Massingue, B., Mdala, H., Mutamina, D., et al., 2016. Passive rifting of thick lithosphere in the southern East African Rift: evidence from mantle transition zone discontinuity topography. J. Geophys. Res. Solid Earth 121 (11), 8068–8079. https://doi.org/10.1002/2016JB013131.

Reed, C.A., Liu, K.H., Yu, Y., Gao, S.S., 2017. Seismic anisotropy and mantle dynamics beneath the Malawi Rift Zone, East Africa. Tectonics 36 (7), 1338–1351. https://doi.org/10.1002/2017TC004519.

Ritsema, J., van Heijst, H.J., Woodhouse, J.H., 1999. Complex shear wave velocity structure imaged beneath Africa and Iceland. Science 286 (5446), 1925–1928. https://doi.org/10.1126/science.286.5446.1925.

Roberts, E.M., Stevens, N.J., O'Connor, P.M., Dirks, P.H.G.M., Gottfried, M.D., Clyde, W.C., et al., 2012. Initiation of the western branch of the East African Rift coeval with the eastern branch. Nat. Geosci. 5 (4), 289. https://doi.org/10.1038/ngeo1432.

Roecker, S., Ebinger, C., Tiberi, C., Mulibo, G., Ferdinand-Wambura, R., Mtelela, K., et al., 2017. Subsurface images of the Eastern Rift, Africa, from the joint inversion of body waves, surface waves and gravity: investigating the role of fluids in early-stage continental rifting. Geophys. J. Int. 210 (2), 931–950. https://doi.org/10.1093/gji/ggx220.

Sarafian, E., Evans, R.L., Abdelsalam, M.G., Atekwana, E., Elsenbeck, J., Jones, A.G., Chikambwe, E., 2018. Imaging Precambrian lithospheric structure in Zambia using electromagnetic methods. Gondwana Res. 54, 38–49. https://doi.org/10.1016/j.gr.2017.09.007.

Saria, E., Calais, E., Stamps, D.S., Delvaux, D., Hartnady, C.J.H., 2014. Present-day kinematics of the East African Rift. J. Geophys. Res. Solid Earth 119 (4), 3584–3600. https://doi.org/10.1002/2013JB010901.

Sengor, A.M., Burke, K., 1978. Relative timing of rifting and volcanism on Earth and its tectonic implications. Geophys. Res. Lett. 5 (6), 419–421. https://doi.org/10.1029/GL005i006p00419.

Silver, P.G., Gao, S.S., Liu, K.H., Kaapvaal Seismic Group, 2001. Mantle deformation beneath southern Africa. Geophys. Res. Lett. 28 (13), 2493–2496. https://doi.org/10.1029/2000GL012696.

Stamps, D.S., Flesch, L.M., Calais, E., Ghosh, A., 2014. Current kinematics and dynamics of Africa and the East African Rift System. J. Geophys. Res. Solid Earth 119 (6), 5161–5186. https://doi.org/10.1002/2013JB010717.

Stamps, D.S., Iaffaldano, G., Calais, E., 2015. Role of mantle flow in Nubia-Somalia plate divergence. Geophys. Res. Lett. 42 (2), 290–296. https://doi.org/10.1002/2014GL062515.

Stamps, D.S., Saria, E., Kreemer, C., 2018. A geodetic strain rate model for the East African Rift system. Sci. Rep. 8 (1), 732. https://doi.org/10.1038/s41598-017-19097-w.

Stein, S., Stein, C.A., Elling, R., Kley, J., Keller, G.R., Wysession, M., et al., 2018. Insights from North America's failed Midcontinent Rift into the evolution of continental rifts and passive continental margins. Tectonophysics 744, 403–421. https://doi.org/10.1016/j.tecto.2018.07.021.

Stuart, G.W., Bastow, I.D., Ebinger, C.J., 2006. Crustal structure of the northern Main Ethiopian Rift from receiver function studies. Geol. Soc. Lond., Spec. Publ. 259 (1), 253–267. https://doi.org/10.1144/GSL.SP.2006.259.01.20.

Tepp, G., Ebinger, C.J., Zal, H., Gallacher, R., Accardo, N., Shillington, D.J., et al., 2018. Seismic anisotropy of the upper mantle below the Western rift, East Africa. J. Geophys. Res. Solid Earth 123, 5644–5660. https://doi.org/10.1029/2017JB015409.

Wang, T., Feng, J., Liu, K.H., Gao, S.S., 2019. Crustal structure beneath the Malawi and Luangwa rift zones and adjacent areas from ambient noise tomography. Gondwana Res. 67, 187–198. https://doi.org/10.1016/j.gr.2018.10.018.

Yeck, W.L., Sheehan, A.F., Schulte-Pelkum, V., 2013. Sequential H-κ stacking to obtain accurate crustal thicknesses beneath sedimentary basins. Bull. Seismol. Soc. Am. 103 (3), 2142–2150. https://doi.org/10.1785/0120120290.

Yu, Y., Song, J., Liu, K.H., Gao, S.S., 2015. Determining crustal structure beneath seismic stations overlying a low-velocity sedimentary layer using receiver functions. J. Geophys. Res. Solid Earth 120 (5), 3208–3218. https://doi.org/10.1002/2014JB011610.

Yu, Y., Gao, S. S., Zhao, D., Liu, K. H., 2020. Mantle structure and flow beneath an early-stage continental rift: constraints from P wave anisotropic tomography. *Tectonics*, 39(2), e2019TC005590. doi:https://doi.org/10.1029/2019TC005590.

Zhu, L., Kanamori, H., 2000. Moho depth variation in southern California from teleseismic receiver functions. J. Geophys. Res. Solid Earth 105 (B2), 2969–2980. https://doi.org/10.1029/1999JB900322.